

DMODE: Differential Monocular Object Distance Estimation Module without Class Specific Information

Pedram Agand¹, Michael Chang¹, and Mo Chen¹

Abstract—Utilizing a single camera for measuring object distances is a cost-effective alternative to stereo-vision and LiDAR. Although monocular distance estimation has been explored in the literature, most existing techniques rely on object class knowledge to achieve high performance. Without this contextual data, monocular distance estimation becomes more challenging, lacking reference points and object-specific cues. However, these cues can be misleading for objects with wide-range variation or adversarial situations, which is a challenging aspect of object-agnostic distance estimation. In this paper, we propose DMODE, a class-agnostic method for monocular distance estimation that does not require object class knowledge. DMODE estimates an object’s distance by fusing its fluctuation in size over time with the camera’s motion, making it adaptable to various object detectors and unknown objects, thus addressing these challenges. We evaluate our model on the KITTI MOTs dataset using ground-truth bounding box annotations and outputs from TrackRCNN and EagerMOT. The object’s location is determined using the change in bounding box sizes and camera position without measuring the object’s detection source or class attributes. Our approach demonstrates superior performance in multi-class object distance detection scenarios compared to conventional methods.

I. INTRODUCTION

For AI-enabled object detection, applications in simultaneous localization and mapping (SLAM), virtual reality, surveillance video perception and autonomous vehicles, real-time and precise estimation of object distances is crucial for safe and efficient navigation [1]–[4]. Traditionally, distance estimation is performed using stereo or multi-camera imaging systems or LiDAR measurements, both of which have their own limitations that can impact their use cases and scalability. Stereo imaging requires precise synchronization between two cameras, which can introduce multiple points of failure. Furthermore, stereo vision is limited by the distance between the cameras and the texture of the region of interest [5]. Although accurate, LiDAR systems are considerably more expensive to purchase and operate than a single camera. Moreover, they have several moving parts and components that can fail, and equipping a vehicle with multiple LiDAR devices for redundancy is prohibitively expensive [6]. In contrast, a system that uses a single camera can incorporate several backup cameras for the price of a single LiDAR device, making it more cost-effective and scalable.

However, existing monocular object distance estimation techniques suffer from accuracy issues or labor-intensive data collection requirements. Monocular vision has inherent difficulties in accurately estimating object distances, and

current solutions typically involve a combination of a 2D object detector and a monocular image depth estimator or a monocular 3D object detector [7]. The former approach relies heavily on a monocular depth estimator that is not optimized for precise object-wise depth estimation, while the latter requires additional annotations of 3D bounding box (BBBox) coordinates for training, resulting in specialized equipment and high labeling costs. Consequently, there is a need for a reliable and cost-effective approach that can be easily adapted to new settings and object detectors.

Numerous studies have investigated the use of deep neural networks (DNN) for direct object distance estimation. Early approaches such as inverse perspective mapping (IPM) [8] converted image points into bird’s-eye view coordinates. However, IPM has limitations, especially for distant objects (around 40m) or non-straight roads [9]. Other unsupervised methods include learning from unstructured video sequences [10], employing CNN feature extractors with distance and keypoint regressors [9], and modifying MaskRCNN as demonstrated in [1]. Additionally, a self-supervised framework for fisheye cameras in autonomous driving was enhanced with a multi-task learning strategy [11]. Authors in [12] proposed an end-to-end approach called structured convolutional neural field (SCNF) that combine CNN and continuous condition random field.

The accuracy of class-specific object detection relies on matching the training environment [13]. For example, in a test scenario involving toy objects, a toy car at the same distance as a real car will appear much smaller but may still be detected as a “Car” by object classification networks. Similarly, when an object is presented in the camera field of view while tilted, a class-specific approach can only detect the distance correctly if the object is in the dataset with the exact pose, which is unlikely or requires an enormous dataset. Finally, the precision in class-specific approaches with multiple classes is limited to the accuracy of the classification technique. These limitations don’t affect class-agnostic approaches [14], which don’t require knowledge of expected object sizes at varying distances.

In this paper, we introduce DMODE, a novel approach to object distance estimation that addresses significant challenges. By avoiding reliance on object class information, we prevent the model from memorizing object size patterns at various distances. Instead, DMODE utilizes changes in an object’s projected size over time and camera motion for distance estimation. Our approach achieves three primary contributions: 1) It provides accurate distance estimations without requiring object class information, overcoming the

¹Simon Fraser University, Burnaby, Canada {pagand, michael.chang-7, mochen}@sfu.ca

challenge of class-agnostic estimation. 2) It is independent of camera intrinsic parameters, ensuring adaptability to diverse camera setups. 3) It is able to generalize and accurately estimate distances for unseen object classes, enables efficient transfer learning for new ones, and addresses the challenge of adaptability across different object tracking networks (OTN) and deployment scenarios. To facilitate future studies, the code is available in GitHub at <https://github.com/pagand/distance-estimation>

II. RELATED WORK

A. Monocular depth estimation

Depth estimation has been approached using DNNs, such as continuous condition random fields for image patches proposed by [15]. The accuracy of depth estimation was improved by [16], who incorporated ordinal regression into the depth estimation network and used scale-increasing discretization to convert continuous depth data into an ordinal class vector. These techniques require significant manpower and computing resources, as well as specific training images and corresponding depth maps for each pixel [17]. In the absence of a depth image serving as ground truth (GT), unsupervised training might utilize additional depth cues from stereo images [18] or optical flows [19]. Authors in [20] introduced a novel deep visual-inertial odometry and depth estimation framework to enhance the precision of depth estimation and ego-motion using image sequences and inertial measurement unit (IMU) raw data. However, unsupervised depth estimation methods have inherent scale ambiguity and poor performance due to the lack of perfect GT and geometric constraints [20].

B. Monocular 3D object detection

The challenging task of 3D object recognition from monocular images is related to object distance estimation. Mousavian *et al.* [21] proposed Deep3DBox, which employs a 3D regressor module to estimate the 3D box's dimensions and orientation and takes 2D detection input to crop the input features. To replace the widely used 2D R-CNN architecture, [22] introduced a 3D region proposal network, significantly improving performance. Furthermore, some studies use point cloud detection networks or monocular depth estimation networks as supplementary components of monocular 3D object recognition [23]. These additional details enhance the accuracy of 3D object detection networks.

C. Monocular object distance estimation

Ali and Hussein [24] used a geometric model incorporating camera characteristics and vehicle height as inputs to determine the distance between two cars. Bertoni *et al.* [25] employed a lightweight network to predict human positions from 2D human postures. A generic object distance estimation was developed by adding a depth regression module to the Faster R-CNN-based structure and an additional keypoint regressor to improve performance for objects near the camera [9]. Cai *et al.* [26] proposed a framework that breaks down the problem of monocular 3D object recognition into smaller

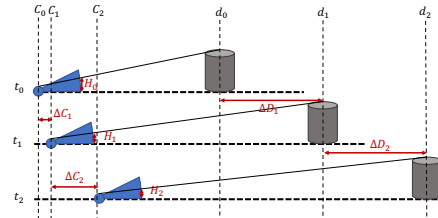


Fig. 1. Simplified 1D DMODE: a mathematical viewpoint

tasks, including object depth estimation, and introduced a height-guided depth estimation technique to address the information loss caused by the 3D to 2D projection. An R-CNN-based network was used to achieve object recognition and distance estimation simultaneously [27].

III. PROBLEM STATEMENT

Our goal is to estimate object distances in 3D by determining their relative Cartesian positions to a single camera without using any class-related information. The camera can be mounted on a moving vehicle or be stationary. For the sake of simplicity, Fig. 1 depicts an illustrative scenario involving camera motion in 1D for three time instants, t_0, t_1, t_2 . Let d_j be the object's distance from the camera, D_j be the object's absolute position, H_j the object's size as captured by the camera, and C_j the camera's absolute position at time t_j . We define $\Delta F_j = F_j - F_{j-1}$, where F can be any of the aforementioned variables. Our objective is to compute d_2 , the object's relative position with respect to the camera at the current (latest) time, given $H_0, H_1, H_2, \Delta C_1, \Delta C_2$.

Here are the assumptions: 1) The distance between the object and the camera in the captured frames varies, which can be caused by the movement of the object, camera, or both. 2) The camera's movement is measured by an IMU [28]. 3) Within the captured frames, the object does not have a pitch rate (rotation around a horizontal axis perpendicular to the line connecting the camera and the object).

IV. METHOD

The framework is depicted in Figure 2. Our method involves tracking the projected size of an object in the camera lens over a predefined time frame while taking into account the camera's motion to estimate the object's distance from the camera. To achieve this, we require an OTN and an IMU for the camera. The distance to the object with constant velocity can be analytically computed using the following relation:

$$d = \frac{H_0 H_1 (\Delta C_1 - \Delta C_2)}{H_2 \Delta H_1 - H_0 \Delta H_2}, \quad (1)$$

where H_i, C_i are the object pixel height and camera location at i -th sequence, and $\Delta X_i = X_i - X_{i-1}$ for $X \in \{H, C\}$. In Sec. IV-A, to demonstrate the model-agnosticity, we derive a mathematical expression for calculating the distance to a 3D object with any dynamic movement of order q and unknown parameters. This analytical proof will illustrate that, to determine the distance to an object with sufficient frames (i.e., $q + 1$ frames), there is no requirement for

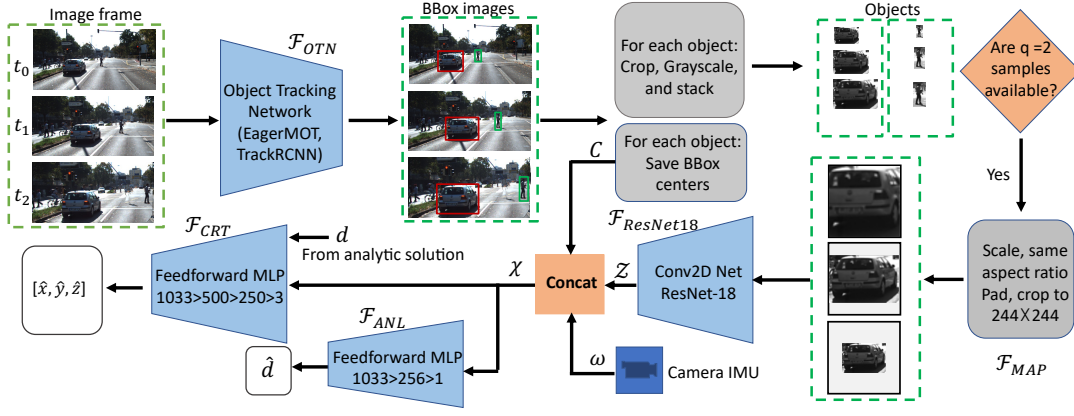


Fig. 2. DMODE framework: workflow of data and models. Only the blue color elements are trainable. The green dots show stack of data.

information about the object's class or shape. In reality, all the required variables in Eq. (1) are measured with noise. The inconsistency between the height measurements is limited by the accuracy of the bounding box and the OTN. Therefore in Sec. IV-B and C, we propose an architectural design and learning framework that makes the use of bounding boxes and ego motion for depth estimation more robust.

A. Theoretical analysis

By extending Fig. 1 to 3D, we aim to determine a function that outputs the relative coordinates of the object $\phi = (x, y, z)$ with respect to the camera. For convenience, suppose $\Delta t = t_2 - t_1 = t_1 - t_0$ and $C_0 = 0$.

$$\phi = \mathcal{F}(H_1, H_2, \dots, H_{q+1}, \Delta C_1, \Delta C_2, \dots, \Delta C_q), \quad (2)$$

where $q + 1$ is the number of input frames and \mathcal{F} is an unknown function need to be determined. To alleviate the effects of noisy measurements and potential errors in OTN, we utilize a DNN to derive \mathcal{F} . The distance to the object is calculated using $d = \sqrt{x^2 + y^2 + z^2}$. For the sake of illustration, we derive the distance for the simplified 1D scenario as shown in Fig. 1.

Axiom: Object projected image size and the distance to camera are inversely proportional [29]

$$\frac{d_{n-1}}{d_n} = \frac{H_n}{H_{n-1}} \doteq P_n \quad (3)$$

Theorem: Given $q + 1$ frames, the following relations apply for all $i \in \{1, 2, \dots, q\}$:

$$(1 - p_i) \sum_{k=i+1}^{q+1} \Delta D_k + \Delta D_i = \sum_{k=i}^q \Delta C_k - p_i \sum_{k=i+1}^q \Delta C_k \quad (4)$$

where $d_j = \Delta C_j = 0, \forall j > q$.

Proof: According to Fig. 1, we have:

$$d_n = d_{n-1} + \Delta D_n - \Delta C_n \quad (5)$$

First let us prove the last relation ($i = q$) in (4). By using Eq. (3) for $n = q$, we have $d_{q-1} = p_q d_q$, which can be

substituted in (5) for $n = q$. This proves the last relation in (4) ($i = q$), since $\Delta D_{q+1} = d_q$, we have:

$$p_q = \frac{d_q - \Delta D_q + \Delta C_q}{d_q} \quad (6)$$

Now for $i = q - 1$, we can write similar relation to (6) as follows by considering the previous time step and substituting d_{q-1}, d_{q-2} using (3) for $n = q, q - 1$:

$$d_q p_q = p_{q-1} d_q p_q + \Delta D_{q-1} - \Delta C_{q-1} \quad (7)$$

Using the relation for p_q in (6), we can simplify the relation in (7) as follows:

$$(d_q - \Delta D_q + \Delta C_q)(1 - p_{q-1}) = \Delta D_{q-1} - \Delta C_{q-1} \quad (8)$$

which is equivalent to the second last relation in (4) ($i = q - 1$). The proof for other relations follows the same pattern. Now we need to integrate the assumption about object movement into ΔD_j variables to reduce one of them as unknown variable (i.e for object with constant velocity we have $\Delta D = V\Delta t$ or with constant acceleration, $\Delta D = 1/2a\Delta t^2 + V\Delta t$). The general relation is as follows:

$$\underline{A}(P)[d_q, \underline{f}]^T = \underline{b}(C, P) \quad (9)$$

where \underline{A} is a $q \times q$ matrix of (P_1, \dots, P_q) parameters, \underline{f} is a row vector of relative movement components (e.g. velocity, acceleration, etc), and \underline{b} is a column vector of $(P_1, C_1, \dots, P_q, C_q)$ parameters. The analytic solution to derive distance in Eq. (9) is given by:

$$d_q = \underline{A}_1^{-1} \underline{b}(C, P) \quad (10)$$

where \underline{A}_1^{-1} is the first row of \underline{A} inverse. ■

For a special case, where the objects of interest is stationary ($q = 1$), the relation will be simplified to:

$$(1 - p_1)d_1 = \Delta C_1, \quad \text{if } q = 1 \quad (11)$$

By assuming objects moving with constant velocity ($q = 2$), we have $\Delta D_1 = \Delta D_2 = \Delta D$ and Eq. (9) is updated as:

$$\begin{bmatrix} P_1 - 1 & 2 - P_1 \\ P_2 - 1 & 1 \end{bmatrix} \begin{bmatrix} d_2 \\ \Delta D \end{bmatrix} = \begin{bmatrix} \Delta C_1 + \Delta C_2 - P_1 \Delta C_2 \\ \Delta C_2 \end{bmatrix} \quad (12)$$

Where we can solve for d_2 and ΔD .

$$d_2 = \frac{\Delta C_1 - \Delta C_2}{P_1 P_2 - 2P_2 + 1}, \quad \text{if } q = 2 \quad (13)$$

This means that analytically, if the object is moving with constant velocity, the camera should not be moved with a constant velocity. However, as mentioned before, upon inspection of the GT annotations, the change of an object’s BBox size is often inconsistent with its distance changes from the camera. Replacing P_1 and P_2 with its definition given in Eq. (6), proves Eq. (1).

B. Network architecture

As shown in Fig. 2, the sequential network, inspired from [30], consist of a 2D convolutional neural network (CNN) and three multi-layer perceptrons (MLPs) with batch normalization implemented between each layer. After processing the detected object from OTN (\mathcal{F}_{OTN}), three consecutive frames are stacked and passed through a mapping function (\mathcal{F}_{MAP}) comprised of an MLP with a soft-plus activation function. As shown in the upper right corner of Fig. 2, upon the availability of 3 frames of an object, we resize and crop them to the size of 224×224 . We employ ResNet-18 ($\mathcal{F}_{ResNet18}$) [31] by inputting selected bounding box (BBox) information to yield 1000 parameters as latent variables (\mathcal{Z}).

$$\begin{aligned} B_{t_i} &= \mathcal{F}_{OTN}(I_{t_i}); \quad \forall i \in \{0, 1, 2\}, \\ S_t &= \mathcal{F}_{map}(B_{t_1}, B_{t_2}, B_{t_3}), \\ \mathcal{Z}_{(1 \times 1000)} &= \mathcal{F}_{ResNet18}(S_t), \end{aligned} \quad (14)$$

where, I_{t_i} and B_{t_i} represent the image frame and the BBox information in the time frame t_i , respectively. Additionally, S_t is the stacked processed BBox image after applying the mapping. The latent variables are then concatenated with an additional 33 variables to create BBox features. These variables encompass the camera’s Cartesian velocities, accelerations, and angular accelerations of the three keyframes ($\omega_{(1 \times 27)}$). The remaining parameters are the object’s BBox centers relative to the image dimensions ($C_{(1 \times 6)}$), which are the only BBox information not related to their class. The BBox features ($\mathcal{X}_{(1 \times 1033)} = [\mathcal{Z}, C, \omega]$) are fed to another MLP to derive three separate parameters in Cartesian space ($[x, y, z] = \mathcal{F}_{CRT}(\mathcal{X}, d)$). To enforce the computed analytical solution for d , we use a separate head with an MLP and ReLU to enrich the BBox features ($\hat{d} = \mathcal{F}_{ANL}(\mathcal{X})$). The reason for predicting Cartesian space separately is to allow the model to distinguish between different spatial coordinates and ultimately enhance the overall performance. Additionally, directly learning d with \mathcal{F}_{ANL} will update the bottleneck node (\mathcal{X}) in the backpropagation direction.

C. Learning rules

Upon object detection in any frame, the cached data is examined. If detection data for this object exists for all keyframes, it is prepared by \mathcal{F}_{map} for the following stages: The system crops the detected objects along their BBoxes and converts them into single-channel grayscale images. For

each object, the system collects the corresponding images, and BBox information for the keyframes. The triplet of images is then resized relative to the heights of their BBoxes while maintaining their original aspect ratios. The largest image among the three is scaled to a height of 224, and all three images are padded/cropped to a size of 224×224 . Subsequently, they are overlaid at the center in the order of detections, forming a new 3-channel image that serves as the 2D input to $\mathcal{F}_{ResNet18}$. It is important to note that \mathcal{F}_{OTN} in Eq. (14) is a pre-trained network, \mathcal{F}_{map} is an arithmetic manipulation, and only $\mathcal{F}_{ResNet18}$, \mathcal{F}_{CRT} , and \mathcal{F}_{ANL} are trained concurrently. The objective function is based on the robust Adaptive Reverse Huber Loss (BerHu) [32]:

$$B(\phi, \phi^*) = \begin{cases} |\phi - \phi^*|, & \text{if } |\phi - \phi^*| \leq c, \\ \frac{(\phi - \phi^*)^2 + c^2}{2c}, & \text{otherwise} \end{cases} \quad (15)$$

where, ϕ^* represents the corresponding GT of Cartesian space, and $c = 0.2 \cdot \max(|\phi - \phi^*|)$. The BerHu loss function integrates L_1 and L_2 features and adapts according to the c value. Contrary to the L_2 loss function, the BerHu loss function converges more rapidly while effectively preserving small residuals, as it is differentiable at the point c where the transition between L_1 and L_2 losses takes place. This enables the network to leverage the shrinkage power of L_1 norm, thereby avoiding low gradients for relatively small residuals. The final loss inspired from multi-task training in [33] is defined as follows:

$$L = \frac{1}{4N} \sum_{i=1}^N (B(x_i, x_i^*) + B(y_i, y_i^*) + B(z_i, z_i^*) + B(d_i, d_i^*)), \quad (16)$$

where N represents the number of mini-batch samples, and i is the index of all images for the current batch. We utilized the ADAM optimizer with a weight decay of $1e-5$. To prevent over-fitting, we implemented dropout and batch normalization approach [34], [35].

V. RESULTS

A. Model setup

Our model capitalizes on the evolution of an object’s size over time, paired with camera movements, to estimate distances. We employ a 3-interval scheme, mathematically presuming constant velocity. To discern a noticeable difference, we have chosen a 1-second look-back time frame. The keyframes for this scheme will be frames n , $n - 5$, and $n - 10$, corresponding to t_2 , t_1 , and t_0 , respectively, given that KITTI’s camera records at 10 frames per second. For our dataset, we utilize the images, annotations, and IMU data from the KITTI Multi Object Tracking dataset [36]. This dataset includes detection, classification, and tracking data for seven categories. We omit object detections labeled as “Misc” or “DontCare” from the KITTI dataset. Furthermore, we filter out all entries where the object is not entirely within the frame, and disregard object detections with bounding boxes touching the frame’s edge during testing. To ensure

consistency across images, occluded object detections are not included in the training process. The size of objects is determined using the height of their bounding boxes (BBboxes). Our training and validation split adheres to the data separation employed by TrackRCNN (TRCNN) and EagerMOT (EMOT). We base our results on the validation set, with each model trained over 100 epochs, a batch size of 32, and a learning rate of $1e-3$. We estimate distances to the centers of objects, as defined by KITTI’s 3D BBox annotations, rather than the point closest to the camera.

To evaluate our method, we use the following common metrics. Each metric has a corresponding mark where \downarrow means “lower is better” and \uparrow means “higher is better”. 1) Median relative error $MRE \downarrow = \text{Median}(\|d_1^* - d_1\|, \dots, \|d_n^* - d_n\|)$ 2) Absolute relative error $AbsRel \downarrow = \frac{1}{N} \sum \left(\frac{\|d_i^* - d_i\|}{d_i} \right)$ 3) Square relative error $SquirRel \downarrow = \frac{1}{N} \sum \left(\frac{\|d_i^* - d_i\|^2}{d_i} \right)$ 4) Threshold $\delta \uparrow = \max(d_i/d_i^*, d_i^*/d_i)\% < 1.25$ 5) confidence interval $.95CI \downarrow = Rel.Err. \pm x$ 6) Root mean square error $RMSE \downarrow = \sqrt{\frac{1}{N} \sum \|d_i^* - d_i\|^2}$ 7) $RMSE_{\log} \downarrow = \sqrt{\frac{1}{N} \sum \|\log d_i^* - \log d_i\|^2}$

To assess our method’s robustness across diverse data sources, we tested it using TRCNN [37] and EMOT [38]. However, a limitation arises from these OTNs, which only detect cars and pedestrians, while KITTI annotations encompass seven object classes. The unique identifiers assigned by the OTN sometimes differ from those in the GT annotations. To assign GT distances to OTN-detected objects in each frame, we compare the OTN’s BBox outputs with GT BBboxes. The GT annotation is assigned to one of the OTN’s outputs if it maximizes the following formula among all detections ($BOX_{pred} \cap BOX_{GT} - BOX_{pred} \oplus BOX_{GT}$).

B. Comparison

We compared our method with baselines in Table I. Our model was trained using EMOT as the OTN on the full set of GT annotations for all evaluation scenarios. Among recent literature, only SVR [7], IPM [8], and Enhanced res50/vgg16 [9] provided their single-class evaluations. The accuracy measurements for IPM and SVR were taken from Zhu and Fang experiments [9]. In single-class evaluations for cars, our model performed better in AbsRel, threshold, and $RMSE_{\log}$, while performing worse in SquirRel and RMSE. This suggests that while our model is more accurate on average, it exhibits more extreme outliers. For pedestrians, our approach surpassed all other methods that provided their single-class evaluation. In terms of multi-class training, our model outperformed all of these methods across all metrics. We not only surpassed the performance of [9]’s non-class-specific model but also outperformed their model that utilized a classifier. We additionally include two other approaches: SCNF [12] and SynDistNet (ResNet-50) [11], both of which only provided their multi-class evaluation. SynDistNet results were obtained from an experiment conducted by Liang *et al.* [39]. Although our approach is designed to perform well

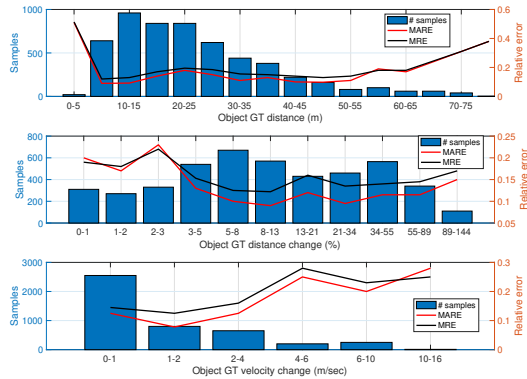


Fig. 3. Error bar in relation to distances, velocity, and acceleration. The red and black lines respectively represents AbsRel and MRE.

with under-specified or unknown classes, it still outperforms these approaches in terms of AbsRel, RMSE and $RMSE_{\log}$ for the KITTI dataset and performs comparably in other metrics. We interpret this performance as resulting from high penalties applied to objects too far away, where their relative changes in two frames are not noticeable.

VI. ABLATION STUDIES

A. Dataset robustness testing

Table II presents the model’s performance when tested on the full annotation of the validation set. To evaluate our method’s robustness regarding the dataset, we assessed the model’s performance when fed different sources of detections of the validation set. The model was initially trained on the full annotations of the GT training set. As EMOT and TRCNN only detect “Cars” and “Pedestrians”, we included the class-limited GT results as a baseline (GT^*). Furthermore, to evaluate the model’s ability to transfer learning across different object detection systems, we present our model’s performance when it was trained and tested on TRCNN’s outputs, as shown in the last row of Table II.

B. Class agnostic testing

As the employed OTN only tracks cars and pedestrians, and to make our results comparable to other literature, we attempted to test class agnosticism by removing the “Car” class from the dataset and evaluating its performance during testing. Table III demonstrates our method’s performance in estimating the distances of cars, even though they were not part of the training set. It also illustrates the accuracy improvement through transfer learning (TL) when the previously missing class is included in the training data. Therefore, our approach provides more accurate results for classes that were never encountered in the training dataset compared to non-model-agnostic rivals that provide better individual class predictions for known classes.

C. Discussion

Often, a trade-off exists between versatility and specialization. Class-agnostic methods excel in versatility, accommodating a wide array of objects without requiring knowledge

TABLE I
COMPARISON BETWEEN BASELINES AND OUR METHOD.

Class type	Method	$\delta < 1.25 \uparrow$	AbsRel \downarrow	SquirRel \downarrow	RMSE \downarrow	RMSE _{log} \downarrow
Car only	SVR [7]	0.345	1.494	47.748	18.970	1.494
	IPM [8]	0.701	0.497	1290.509	237.618	0.451
	Enhanced res50 [9]	0.796	0.188	0.843	4.134	0.256
	Enhanced vgg16 [9]	0.848	0.161	0.619	3.580	0.228
	Ours	0.849	0.107	0.998	4.931	0.173
Pedestrian only	SVR [7]	0.129	1.499	34.561	21.677	1.260
	IPM [8]	0.688	0.340	543.223	192.177	0.348
	Enhanced res50 [9]	0.734	0.188	0.807	3.806	0.225
	Enhanced vgg16 [9]	0.747	0.183	0.654	3.439	0.221
	Ours	0.842	0.109	0.635	3.110	0.149
Average on Multiple classes	Zhou (ResNet-50) [10]	0.678	0.208	1.768	6.856	0.283
	Enhanced res50 [9]	0.550	0.271	2.363	8.166	0.336
	Enhanced vgg16 [9]	0.629	0.251	1.844	6.870	0.314
	SynDistNet (ResNet-50) [11]	0.896	0.109	0.718	4.516	0.180
	SCNF [12]	0.775	0.184	0.842	9.773	0.311
Ours	0.847	0.108	0.872	4.382	0.165	

TABLE II
MODEL TRAINED AND TESTED ON GT OR OTN

Train type	Test type	AbsRel \downarrow	MRE \downarrow	.95CI \downarrow	RMSE \downarrow
GT	GT	0.145	0.107	3.9e-3	6.765
GT	<i>GT*</i>	0.138	0.107	3.2e-3	6.676
GT	TRCNN	0.168	0.125	4.6e-3	7.139
GT	E-MOT	0.160	0.124	3.7e-3	6.435
TRCNN	TRCNN	0.163	0.118	4.8e-3	7.202

TABLE III
MODELS TESTED ON GT WITH CAR ONLY CLASS

Model	Train class	AbsRel \downarrow	MRE \downarrow	.95CI \downarrow	RMSE \downarrow
Enhanced vgg16 [9]	All	0.148	0.101	3.8e-3	5.953
	No Car	0.578	0.534	9.8e-3	21.773
	TL	0.307	0.213	5.6e-3	10.487
Ours	All	0.143	0.113	4.1e-3	7.821
	No Car	0.282	0.243	6.6e-3	13.923
	TL	0.173	0.133	4.9e-3	9.356

of specific classes. This adaptability is crucial in scenarios with diverse and unexpected objects. Conversely, specialized class-aware methods may perform admirably in specific situations but could struggle with unfamiliar objects or scenarios.

Dataset robustness show that our method, trained on GT annotations, can perform well with various OTNs, with minimal accuracy loss. Additionally, training the model on the specific OTN outputs used during testing yields similar accuracy to training on GT annotations. These results indicate our model’s suitability for deployment across diverse systems with different OTNs, maintaining high accuracy without the need for retraining. In class-agnostic testing, our method showed a notably smaller accuracy decrease (97% increase in AbsRel) for unseen object classes compared to Enhanced vgg16 (290% increase in AbsRel), indicating our model’s reduced dependency on class-specific training data.

Fig. 3 displays error bars in a histogram for different object distances, velocities, and accelerations. Our method excelled for objects within the 5 to 60-meter range, where most detections occurred. The error spike within 5 meters is due to limited training samples, as truncated objects were excluded from training. Beyond 60 meters, error increased due to camera resolution limitations and challenges in representing size changes in the 2D input. The analysis of the second subplot in Fig. 3 indicates our model’s effectiveness increases for objects with significant relative distance changes from the camera compared to those with minimal changes, resulting in a noticeable 3-5% accuracy improvement. However, it’s important to note that the 3-interval version of our method is only suitable for objects moving at a constant velocity, as discussed in the mathematical motivation section. In the third subplot, we find that our model maintains accuracy for objects with velocity changes below 2m/s but experiences a decline in performance for objects with greater motion variations. Fortunately, most objects in scenarios like city driving, as captured in the KITTI dataset, do not exhibit velocity changes exceeding 2m/s. Consequently, our current model provides distance estimations with an average relative error of 13.5%, despite its limitations.

VII. CONCLUSION

We introduced a class-agnostic method for object distance estimation, leveraging the object’s evolving appearance and camera motion. This property enables TL with target class samples, yielding satisfactory multi-class distance estimation. The limitation of our approach includes time delay and accurate object tracking over three key frames, matching the training intervals, is essential. Moreover, The network architecture currently employs three input channels, suitable for constant object velocity. While results are generally good, outliers may occur for rapidly changing objects. Future work may involve increasing the channel capacity of our 2D network to improve performance in such cases.

REFERENCES

- [1] Y. Zhang, Y. Li, M. Zhao, and X. Yu, "A regional regression network for monocular object distance estimation," in *2020 IEEE International Conference on Multimedia & Expo Workshops (ICMEW)*. IEEE, 2020, pp. 1–6.
- [2] P. Agand, A. Iskvov, and M. Chen, "Deep reinforcement learning-based intelligent traffic signal controls with optimized co2 emissions," in *2023 IEEE/RSJ International Conference on Intelligent Robots and Systems (IROS)*. IEEE, 2023, pp. 5495–5500.
- [3] X. Yang, H. Luo, Y. Wu, Y. Gao, C. Liao, and K.-T. Cheng, "Reactive obstacle avoidance of monocular quadrotors with online adapted depth prediction network," *Neurocomputing*, vol. 325, pp. 142–158, 2019.
- [4] R. Kang, J. Shi, X. Li, Y. Liu, and X. Liu, "Df-slam: A deep-learning enhanced visual slam system based on deep local features," *arXiv preprint arXiv:1901.07223*, 2019.
- [5] A. Saxena, J. Schulte, A. Y. Ng, et al., "Depth estimation using monocular and stereo cues," in *IJCAI*, vol. 7, 2007, pp. 2197–2203.
- [6] D. Reyes Duran, E. Robinson, A. J. Kornecki, and J. Zalewski, "Safety analysis of autonomous ground vehicle optical systems: Bayesian belief networks approach," in *2013 Federated Conference on Computer Science and Information Systems*, 2013, pp. 1419–1425.
- [7] F. Gökçe, G. Üçoluk, E. Şahin, and S. Kalkan, "Vision-based detection and distance estimation of micro unmanned aerial vehicles," *Sensors*, vol. 15, no. 9, pp. 23 805–23 846, 2015. [Online]. Available: <https://www.mdpi.com/1424-8220/15/9/23805>
- [8] S. Tuohy, D. O’Cualain, E. Jones, and M. Glavin, "Distance determination for an automobile environment using inverse perspective mapping in opencv," in *IET Irish Signals and Systems Conference (ISSC 2010)*, 2010, pp. 100–105.
- [9] J. Zhu and Y. Fang, "Learning object-specific distance from a monocular image," in *Proceedings of the IEEE/CVF International Conference on Computer Vision*, 2019, pp. 3839–3848.
- [10] T. Zhou, M. Brown, N. Snavely, and D. G. Lowe, "Unsupervised learning of depth and ego-motion from video," in *Proceedings of the IEEE conference on computer vision and pattern recognition*, 2017, pp. 1851–1858.
- [11] V. R. Kumar, M. Klingner, S. Yogamani, S. Milz, T. Fingscheidt, and P. Mader, "Syndistnet: Self-supervised monocular fisheye camera distance estimation synergized with semantic segmentation for autonomous driving," in *Proceedings of the IEEE/CVF winter conference on applications of computer vision*, 2021, pp. 61–71.
- [12] Y. Shi, T. Lin, B. Chen, R. Wang, and Y. Zhang, "Structured deep learning based object-specific distance estimation from a monocular image," *International Journal of Machine Learning and Cybernetics*, pp. 1–11, 2023.
- [13] P. Agand, M. Chen, and H. D. Taghirad, "Online probabilistic model identification using adaptive recursive mcmc," in *2023 International Joint Conference on Neural Networks (IJCNN)*. IEEE, 2023, pp. 1–8.
- [14] P. Agand and M. A. Shoorehdeli, "Adaptive model learning of neural networks with uub stability for robot dynamic estimation," in *2019 International Joint Conference on Neural Networks (IJCNN)*. IEEE, 2019, pp. 1–6.
- [15] F. Liu, C. Shen, G. Lin, and I. Reid, "Learning depth from single monocular images using deep convolutional neural fields," *IEEE transactions on pattern analysis and machine intelligence*, vol. 38, no. 10, pp. 2024–2039, 2015.
- [16] H. Fu, M. Gong, C. Wang, K. Batmanghelich, and D. Tao, "Deep ordinal regression network for monocular depth estimation," in *Proceedings of the IEEE conference on computer vision and pattern recognition*, 2018, pp. 2002–2011.
- [17] J. Zhang, Q. Su, C. Wang, and H. Gu, "Monocular 3d vehicle detection with multi-instance depth and geometry reasoning for autonomous driving," *Neurocomputing*, vol. 403, pp. 182–192, 2020.
- [18] C. Godard, O. Mac Aodha, and G. J. Brostow, "Unsupervised monocular depth estimation with left-right consistency," in *Proceedings of the IEEE conference on computer vision and pattern recognition*, 2017, pp. 270–279.
- [19] C. Godard, O. Mac Aodha, M. Firman, and G. J. Brostow, "Digging into self-supervised monocular depth estimation," in *Proceedings of the IEEE/CVF International Conference on Computer Vision*, 2019, pp. 3828–3838.
- [20] Y. Wan, Q. Zhao, C. Guo, C. Xu, and L. Fang, "Multi-sensor fusion self-supervised deep odometry and depth estimation," *Remote Sensing*, vol. 14, no. 5, p. 1228, 2022.
- [21] A. Mousavian, D. Anguelov, J. Flynn, and J. Kosecka, "3d bounding box estimation using deep learning and geometry," in *Proceedings of the IEEE conference on Computer Vision and Pattern Recognition*, 2017, pp. 7074–7082.
- [22] G. Brazil and X. Liu, "M3d-rpn: Monocular 3d region proposal network for object detection," in *Proceedings of the IEEE/CVF International Conference on Computer Vision*, 2019, pp. 9287–9296.
- [23] Y. You, Y. Wang, W.-L. Chao, D. Garg, G. Pleiss, B. Hariharan, M. Campbell, and K. Q. Weinberger, "Pseudo-lidar++: Accurate depth for 3d object detection in autonomous driving," *arXiv preprint arXiv:1906.06310*, 2019.
- [24] A. A. Ali and H. A. Hussein, "Distance estimation and vehicle position detection based on monocular camera," in *2016 Al-Sadeq International Conference on Multidisciplinary in IT and Communication Science and Applications (AIC-MITCSA)*. IEEE, 2016, pp. 1–4.
- [25] L. Bertoni, S. Kreiss, and A. Alahi, "Monoloco: Monocular 3d pedestrian localization and uncertainty estimation," in *Proceedings of the IEEE/CVF International Conference on Computer Vision*, 2019, pp. 6861–6871.
- [26] Y. Cai, B. Li, Z. Jiao, H. Li, X. Zeng, and X. Wang, "Monocular 3d object detection with decoupled structured polygon estimation and height-guided depth estimation," in *Proceedings of the AAAI Conference on Artificial Intelligence*, vol. 34, 2020, pp. 10 478–10 485.
- [27] Y. Zhang, L. Ding, Y. Li, W. Lin, M. Zhao, X. Yu, and Y. Zhan, "A regional distance regression network for monocular object distance estimation," *Journal of Visual Communication and Image Representation*, vol. 79, p. 103224, 2021.
- [28] P. Agand, M. Motaharifard, and H. D. Taghirad, "Teleoperation with uncertain environment and communication channel: An h_∞ robust approach," in *2017 Iranian Conference on Electrical Engineering (ICEE)*. IEEE, 2017, pp. 685–690.
- [29] P. Alphonse and K. Sriharsha, "Depth perception in single rgb camera system using lens aperture and object size: a geometrical approach for depth estimation," *SN Applied Sciences*, vol. 3, no. 6, pp. 1–16, 2021.
- [30] Y. Fan, P. Agand, M. Chen, E. J. Park, A. Kennedy, and C. Bae, "Sequential modeling of complex marine navigation: Case study on a passenger vessel (student abstract)," in *Proceedings of the AAAI Conference on Artificial Intelligence*, vol. 38, no. 21, 2024, pp. 23 484–23 485.
- [31] K. He, X. Zhang, S. Ren, and J. Sun, "Deep residual learning for image recognition," in *Proceedings of the IEEE conference on computer vision and pattern recognition*, 2016, pp. 770–778.
- [32] S. Lambert-Lacroix and L. Zwald, "The adaptive berhu penalty in robust regression," *Journal of Nonparametric Statistics*, vol. 28, no. 3, pp. 487–514, 2016.
- [33] P. Agand, M. Mahdavian, M. Savva, and M. Chen, "Letfuser: Lightweight end-to-end transformer-based sensor fusion for autonomous driving with multi-task learning," *arXiv preprint arXiv:2310.13135*, 2023.
- [34] P. Agand, A. Kennedy, T. Harris, C. Bae, M. Chen, and E. J. Park, "Fuel consumption prediction for a passenger ferry using machine learning and in-service data: A comparative study," *Ocean Engineering*, vol. 284, p. 115271, 2023.
- [35] C. Garbin, X. Zhu, and O. Marques, "Dropout vs. batch normalization: an empirical study of their impact to deep learning," *Multimedia Tools and Applications*, vol. 79, no. 19, pp. 12 777–12 815, 2020.
- [36] A. Milan, L. Leal-Taixé, I. Reid, S. Roth, and K. Schindler, "Mot16: A benchmark for multi-object tracking," *arXiv preprint arXiv:1603.00831*, 2016.
- [37] P. Voigtlaender, M. Krause, A. Osep, J. Luiten, B. B. G. Sekar, A. Geiger, and B. Leibe, "Mots: Multi-object tracking and segmentation," in *Proceedings of the IEEE/CVF Conference on Computer Vision and Pattern Recognition*, 2019, pp. 7942–7951.
- [38] A. Kim, A. Ošep, and L. Leal-Taixé, "Eagermot: 3d multi-object tracking via sensor fusion," *arXiv preprint arXiv:2104.14682*, 2021.
- [39] H. Liang, Z. Ma, and Q. Zhang, "Self-supervised object distance estimation using a monocular camera," *Sensors*, vol. 22, no. 8, p. 2936, 2022.